Formation Control for the Next Generation Earth-Gravimetry Missions

Published in Proc. 18th IFAC World Congress, Milan (Italy), August 28 - September 2, 2011

Formation control for the next generation Earth-gravimetry missions

Enrico Canuto* Andrés Molano-Jimenez* Carlos Perez-Montenegro* Luca Massotti**

**Politecnico di Torino, Dipartimento di Automatica e Informatica*
Corso Duca degli Abruzzi 24, 10129 Torino, Italy(e-mail: enrico.canuto@polito.it)
*** ESA Earth Observation Future Missions Division,*
ESTEC EOP-SF, Noordwijk NL-220 AG, The Netherlands(e-mail: luca.massotti@esa.int)

Abstract: The formation control of a long-distance, drag-free, low-thrust, low-Earth orbit satellite is outlined, in view of future Earth-gravity monitoring missions employing long baseline interferometry (> 10 km) and lasting at least six years. To this purpose, a formation consisting of two drag-free satellites, orbiting at a fixed distance in a sun-synchronous orbit, has been proposed as a baseline. Formation fluctuations are bounded by a box 500x50x50 m. Although at first sight not demanding, the formation control induces non-gravitational accelerations, that are obliged to respect tight drag-free requirements, and are constrained by millinewton thrust bounds. In addition formation fluctuations due to tide forces should not be impaired as their measurement is the mission goal. Requirements are formulated as four time and frequency–domain inequalities, to be suitably parameterized by control gains. Exploiting close-loop Hill's equation properties and asymptotic approximations, explicit design inequalities are obtained leading to a first-trial control design. Simulated runs through a fine spacecraft and low-Earth-orbit simulation dominated by the highly variable thermosphere drag show the first-trial design meets the tight control requirements, and demonstrates mission feasibility.

Keywords: Satellite formation, drag-free, control, low-thrust, low-Earth-orbit

1. INTRODUCTION

The paper addresses the formation control of a pair of satellites in a low-Earth orbit at a long distance, say > 10 km during a 6-year mission. The distance is fixed by the baseline of an interferometric gradiometer made by the pair of the satellites themselves, which are forced to free fall by cancelling their non gravitational forces (drag-free control). The differential acceleration becomes highly sensible to the local gravity tensor, less non gravitational residuals to be kept below a pre-specified target. The differential acceleration and the gravity tensor parameters are elaborated from the formation fluctuations reckoned by an inter-satellite laser interferometer, and from the satellite drag-free accelerations measured by GOCE-class accelerometers. Laser pointing accuracy is guaranteed by fine satellite alignment (attitude control) and by the formation displacement to stay within a box $500 \times 50 \times 50$ m (formation control). The latter should be considered a tight constraint as is tailored to J2 differential fluctuations (Fig. 3). All-propulsion actuation has been adopted. A layout of ten thrusters (one of them in cold redundancy) has been designed from the heritage of the early GOCE design (Canuto, 2008, Canuto and Massotti, 2009), later abandoned because of immature technology. A pair of redundant mini-thrusters (< 20 mN) is dedicated to along-track drag-free and formation. Eight micro-thrusters (< 1.2 mN) in a balanced configuration are dedicated to lateral formation, drag-free and attitude control. The symmetric configuration allows biasing the thrust. Main limitation comes from a poor throttability range (<10) in front of the wide and unprecedented ratio (up to 40) requested by a long-term drag-free mission at low-Earth orbit. A 6-year drag-free mission must bear the extreme drag conditions of the thermosphere that are driven by variable solar and geomagnetic activities. Throttability may be attenuated by correlating orbit altitude with the expected average solar activity; nevertheless high solar activity is accompanied by wide fluctuations leading to the throttability target of 40. The overall control design, combining drag-free, attitude and formation, must guarantee to stay below thrust upper bound under normal conditions, and to smoothly degrade under thruster saturation.

The paper outlines a formation control design capable of respecting thruster bounds together with formation and drag-free requirements for a total of three norm inequalities (Section 3.1). Formation control perturbs each satellite with a non-gravitational acceleration, to be kept within drag-free limits. Drag-free control is fed by non-gravitational accelerations that are elaborated from the on-board accelerometer data. Formation control is fed by differential GPS range and rate, which are affected by the differential acceleration that includes the differential gravity to be measured by the mission. It is therefore mandatory that the formation command be sufficiently decoupled from gravity components, adding a further norm inequality (the fourth one) to control design. At the author's knowledge, no formation control of this kind has been so far studied (Kapila et al., 2000, Rossi and Lovera, 2002, Xu et al., 2007).

Formation dynamics with stochastic disturbance dynamics (Canuto, 2007, Canuto et al., 2010a) is outlined in Section 2 without proof (Canuto et al, 2011). Following Schweighart and Sedwick (2002) and Hinalhan et al. (2002), it accounts for eccentricity and J2 (Earth flatness) which latter make state equations to be periodic. Due to low eccentricity (<0.5%) control design is afforded in Section 3 with a linear, time-invariant approximation, where periodic terms play the role of input perturbations. The linear control law includes reference command, tracking errors and disturbance rejection, but the focus here is on the design of tracking error gains capable of respecting design inequalities. Reference generator and state predictor are not treated. It is shown that closed-loop eigenvalues can be decoupled, without impairing the tuning/optimizing capability of the feedback gains with respect to the design inequalities. A first-trial and explicit design is shown, based on the series expansion of the periodic input perturbations and on the asymptotic expansion of the closed-loop transfer functions. Design performance is demonstrated by the simulated results in Section 4. The latter ones have been obtained with a fine simulator of the low-Earth-orbit environment making critical long-term missions because of the thermosphere drag.

2. FORMATION DYNAMICS

2.1 *Reference orbit and frame*

The following notations are employed: arrowed letters like $\vec{r}$ denote vectors, bold letters like $\mathbf{r}$ denote Cartesian coordinates in some frame. Formation relative position and rate coordinate vectors (longitudinal Δx, radial Δz and cross-track Δy)

$$\Delta\mathbf{r}^T = \left(\mathbf{r}_0 - \mathbf{r}_1\right)^T = \left[\Delta x \quad \Delta z \quad \Delta y\right],\ \Delta\mathbf{v} = \mathbf{v}_0 - \mathbf{v}_1 \qquad (1)$$

are defined with respect to the Local Orbital Frame (LORF)

$$\left\{\underline{C}, \vec{i}_O = \underline{\vec{v}}/\left|\underline{\vec{v}}\right|, \vec{j}_O = \underline{\vec{r}} \times \underline{\vec{v}}/\left|\underline{\vec{r}} \times \underline{\vec{v}}\right|, \vec{k}_O = \vec{i}_O \times \vec{j}_O\right\}, \qquad (2)$$

which is attached to the drag-free orbit of the formation Centre-of-Mass (CoM) $\underline{C}$. The natural order of the radial and cross-track entries is reversed in (1). The formation CoM is defined by $\underline{\vec{r}} = \left(\vec{r}_0 + \vec{r}_1\right)/2$, where $\vec{r}_k$, $k = 0,1$ denotes the Earth-centered satellite CoM position (Fig. 1).

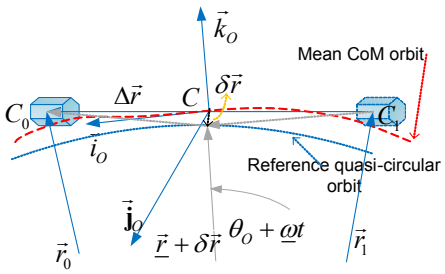

Fig. 1. Formation geometry and local orbital frame.

Orbit and frame are materialized by averaging on-board GPS measurements and retrieving the LORF quaternion $\boldsymbol{q}_O$ through a suitable state predictor. The orbit of $\underline{C}$ is taken as the reference weakly elliptic orbit subject to J2. Notice the actual orbit is subject to a drift $\delta\vec{r} = \left(\delta\vec{r}_0 + \delta\vec{r}_1\right)/2$ in Fig. 1, that is caused by the drag-free residual bias, as a result of the on-board accelerometer offset. The drift $\left|\delta\dot{\vec{r}}\right| \cong 500$ m/day is a common-mode error not affecting formation dynamics. The latter is affected by the differential drift $\delta\vec{r} = \delta\vec{r}_0 - \delta\vec{r}_1$, to be actively rejected as shown below.

2.2 *Formation dynamics and perturbations*

Formation dynamics for a quasi-polar orbit $i \cong \pi/2$, leads to the following linear, time-invariant equation, written with radial and cross-track coordinates in reverse order as in (1):

$$\begin{bmatrix} \Delta\dot{\mathbf{r}} \\ \Delta\dot{\mathbf{v}} \\ \dot{\mathbf{x}}_d \end{bmatrix}(t) = \left[\begin{array}{ccc|c} A_r & I & 0 & \\ -\Omega^2 & A_v & I & \\ \hline 0 & 0 & 0 & \end{array}\right] \begin{bmatrix} \Delta\mathbf{r} \\ \Delta\mathbf{v} \\ \mathbf{x}_d \end{bmatrix}(t) + \begin{bmatrix} 0 \\ I \\ 0 \end{bmatrix}\left(\Delta\mathbf{u} + \mathbf{g}(\theta)\right) + \begin{bmatrix} 0 \\ \mathbf{w}_a \\ \mathbf{w}_d \end{bmatrix}. \qquad (3)$$

Sub-matrices and vectors hold

$$A_r = \begin{bmatrix} 0 & -2\underline{\omega} & 0 \\ 0 & 0 & 0 \\ 0 & 0 & 0 \end{bmatrix}, A_v = \begin{bmatrix} 0 & 0 & 0 \\ 2\underline{\omega} & 0 & 0 \\ 0 & 0 & 0 \end{bmatrix}, \Omega^2 = \begin{bmatrix} 0 & 0 & 0 \\ 0 & \underline{\omega}_z^2 & 0 \\ 0 & 0 & \underline{\omega}_y^2 \end{bmatrix}. \qquad (4)$$

Measurements are provided by on-board differential GPS. The forcing functions are the formation command $\Delta\mathbf{u}$, the periodic function $\mathbf{g}(\theta)$ and the wide-band noise vectors $\mathbf{w}_a, \mathbf{w}_d$ generating the stochastic process

$$\mathbf{d}(t) = \mathbf{x}_d(t) + \mathbf{w}_a(t). \qquad (5)$$

The latter is the sum of a random drift and noise, and accounts for drag-free residuals and thruster noise, according to Canuto et al., 2010a. The command is implemented by dispatching the opposite component to each spacecraft, i.e.

$$\Delta\mathbf{u} = \mathbf{u}_0 - \mathbf{u}_1,\ \mathbf{u}_0 = \Delta\mathbf{u}/2,\ \mathbf{u}_1 = -\mathbf{u}_0\ . \qquad (6)$$

In this way peak command is reduced on both spacecrafts as requested by (11). The differential drag-free residual $\Delta\mathbf{a}$ must include the formation command and is defined by

$$\Delta\mathbf{a}(t) = \mathbf{d}(t) + \Delta\mathbf{u}(t) = \Delta\mathbf{a}_d(t) + \Delta\mathbf{a}_h(\theta). \qquad (7)$$

The last sum in (7) split the residuals into random components $\Delta\mathbf{a}_d$ and periodic components $\Delta\mathbf{a}_h(\theta)$.

The orbit frequencies $\underline{\omega} \cong 1.2$ mrad/s, $\underline{\omega}_z$ and $\underline{\omega}_y$ are slightly discrepant due to J2 and eccentricity. Such discrepancies lead to a long-term beat as shown in Fig. 3. The following lemma is immediate.

Lemma 1. The eigenvalues of (3) are the square root of the diagonal entries of $-\Omega^2$, i.e.

$$\lambda_{x0,x1} = 0,\ \lambda_{z0,z1} = \pm j\underline{\omega}_z,\ \lambda_{y0,y1} = \pm j\underline{\omega}_y. \qquad (8)$$

Lemma 1 shows (3) is unstable.

Formation state predictor and control are designed and implemented around a discrete-time version of (3) as in Canuto, 2010b, where the wide-band noise vectors $\mathbf{w}_a, \mathbf{w}_d$ become discrete-time white noise with bounded variance, and the time unit T is designed such that $\underline{\omega}T << 1$.

2.3 *Actuator layout and bounds*

Drag-free, formation and attitude control has been designed to be all–propulsion, mainly for noise reasons. The thruster assembly is partitioned into a pair of mini-thrusters (one redundant, 0.45 to 18 mN) and eight micro-thrusters (0.05 to 2 mN).

Bounds on the disturbance signals $g_j(\theta) + d_j$ and on the

formation commands Δu_j in (3) are listed in Table 1. It shows that the radial bias is incompatible with the command limits. The force bound in Table 1, row 2.1, is an absolute value restricted to formation axes, which has been computed allocating 20% of the peak thrust to formation. The last row converts force into acceleration through the satellite mass $m = 500$ kg. Thrust allocation in Table 1, rows 2.1 and 2.2, has been traded-off with drag-free and attitude control authority. The disturbance overshoot in Table 1, rows 0.1, 1.2 and 1.3, may be avoided in two ways. Radial accelerometer bias, row 0.1, should be reduced either by re-design or by bias estimation before the drag-free control is activated. Gravity and eccentricity perturbations, rows 1.2 and 1.3, are periodic with $\underline{\omega}$ and of higher order. Formation control should avoid their rejection.

Table 1. Bounds to perturbations and commands

No.	Type (symbol)	Along-track [mN]	Radial [mN]	Cross-track [mN]
0	Generic disturbance d_j			
0.1	Acceler. bias	0.06	6(0.06)	0.06
0.2	Drift	negligible	0.004	negligible
1	Periodic disturbance $> J_2$, $g_i(\theta)$			
1.1	Gravity, $> J_2$	0.5	0.5	0.1
1.2	Gravity, J_2	33	37	negligible
1.3	Eccentricity e	50	negligible	negligible
2	Command Δu_j			
2.1	Force bound	1.5 (mini)	1.2 (micro)	1.2 (micro)
2.2	Acceleration	3	2.4	2.4

3. CONTROL OBJECTIVES AND DESIGN

3.1 *Control objectives*

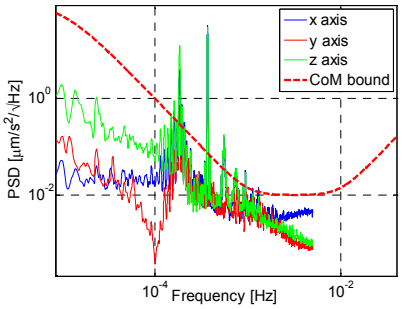

Fig. 2. Spectral density of target and simulated residuals.

Formation objectives assume the drag-free control is operating on each satellite. Drag-free requirements may be relaxed to withstand thruster saturation, whereas formation bounds are assumed to stay fixed. Different than drag-free control where control is fed with the measurements of non gravitational accelerations provided by on-board accelerometers, formation control is fed by differential position and rate, depending on the whole of the differential acceleration: gravity anomalies, eccentricity and drag-free residuals. It implies that formation command may couple with gravitational anomalies, a condition to be avoided inside the mission measurement bandwidth (MBW) defined by

$$f_0 = 1 \text{ mHz} \le f \le f_1 = 10 \text{ mHz}, \tag{9}$$

and corresponding to the minimum of the bowl-shaped profile in Fig. 2. Control objectives are formulated as set of inequalities to be respected by control gains.

1) The formation bound is a time-domain constraint. Define the tracking error $\delta\mathbf{r} = \Delta\mathbf{r} - \Delta\underline{\mathbf{r}}$, with respect to a reference displacement, equal, at the end of the acquisition phase, to $\Delta\underline{\mathbf{r}}^T = [d \;\; 0 \;\; 0]$. The tracking error box is defined by
$$\left|W_r \delta\mathbf{r}\right|_\infty \le \delta r_{\max} = 50 \text{ m}, \; W_r = \text{diag}\{w_{rx} << 1,1,1\}. \tag{10}$$
2) The thrust bound is a time-domain constraint defined by
$$\left|W_u \Delta\mathbf{u}\right|_\infty \le \Delta u_{\max} = 2.4 \; \mu\text{m/s}^2, \; W_u = \text{diag}\{w_{ux} < 1,1,1\}. \tag{11}$$
3) The drag-free bound is a frequency-domain inequality involving the spectral density matrix $\mathbf{S}_a^2(f)$ of the random differential drag-free residuals $\Delta\mathbf{a}_d$ in (7), as follows
$$\sigma_{\max}\left(\mathbf{S}_a^2(f)\right) \le \left|\mathbf{V}_a(jf)\right| \Delta a_{\max}, \; \Delta a_{\max} \le 0.01 \; \mu\text{m/s}^2/\sqrt{\text{Hz}} \tag{12}$$
where $\sigma_{\max}$ is the root of the largest eigenvalue, $\left|\mathbf{V}_a(f)\right| \ge 1$ is bowl-shaped as in Fig. 2 and $\Delta a_{\max}$ is the bound in the MBW.
4) The periodic component $\Delta\mathbf{a}_h$ of the drag-free residuals must decouple from the periodic function $\mathbf{g}(\theta)$ in the MBW
$$\max_f \sigma_{\max}\left(\mathbf{V}(jf)\right) \le \sigma_{h,\max} = 10^{-3}, \; f \ge f_0, \tag{13}$$
where $\mathbf{V}$ is a closed-loop transfer function to be defined in (16), and $\sigma_{\max}$ is the max singular value.

3.2 *The control law*

Following Canuto (2007) and Canuto et al. (2010a), the control law combines tracking and disturbance rejection into

$$\Delta\mathbf{u}(t) = \Delta\underline{\mathbf{u}}(t) - \left(K_r \delta\mathbf{r} + K_v \Delta\mathbf{v} + \mathbf{x}_d\right), \tag{14}$$

where $\Delta\underline{\mathbf{u}}(t) = 0$ as soon as formation acquisition has been obtained, that is assumed here. As a control strategy, the periodic term $\mathbf{g}(\theta)$ does not appear in (14), since it must not be rejected for two different reasons: (i) the eccentricity and J2 components overshoot the thruster bound as shown in Table 1, (ii) periodic components higher than J2 are the mission objective, and must not be cancelled from the formation relative position as entailed by inequality (13). The control design aims to find gain matrices K_r and K_v satisfying the constraints (10) to (13).

The law (14) must be kept as ideal, as actually it is affected by measurement errors through the state predictor, not treated here. On the other hand, the ideal law (14) is not capable of fully rejecting the stochastic disturbance $\mathbf{d}$ in (5) because of causality, leaving the unpredictable noise $\mathbf{w}_a$ to force the tracking error. Notice $\mathbf{w}_a$ includes all unpredictable sources as for instance prediction errors. Closed-loop transfer functions follow from (3) and (14) as

$$\begin{aligned} \Delta\mathbf{a} &= (I - \mathbf{V})\mathbf{w}_a - \mathbf{V}\mathbf{g}, \; \Delta\mathbf{r} = -\mathbf{S}\mathbf{M}(\mathbf{w}_a + \mathbf{g}) \\ \Delta\mathbf{u} &= -\mathbf{V}(\mathbf{w}_a + \mathbf{g}) - s^{-1}\mathbf{w}_d \end{aligned}, \tag{15}$$

where s has been dropped and

$$\mathbf{V}=\mathbf{CSM},\ \mathbf{S}=\left(I+\mathbf{CM}\right)^{-1}, \tag{16}$$

and

$$\mathbf{C}=K_r+K_v s,\ \mathbf{D}_m=\operatorname{diag}\left\{s^2+\underline{\omega}_z^2, s^2+\underline{\omega}_z^2, s^2+\underline{\omega}_y^2\right\}$$
$$\mathbf{M}(s)=\mathbf{D}_m^{-1}(s)\begin{bmatrix}\left(s^2+\underline{\omega}_z^2-4\underline{\omega}^2\right)/s^2 & -2\underline{\omega}/s & 0\\ 2\underline{\omega}/s & 1 & 0\\ 0 & 0 & 1\end{bmatrix}. \tag{17}$$

3.3 Design steps

It is shown how to reduce the four inequalities to a pair and how to formulate their expressions. Time-domain inequalities (10) and (11) are first tackled by expanding tracking errors and command components into a harmonic series of the orbit angular frequency $\underline{\omega}$ as follows

$$\delta\mathbf{r}(t)=\delta\mathbf{r}_d(t)+W_r^{-1}\delta r_{\max}\sum_{k=1}^{\infty}\mathbf{a}_k\sin\left(k\underline{\omega}t+\varphi_k\right)+$$
$$\left\|\sum_{k=1}^{\infty}\left|\mathbf{a}_k\right|\right\|_{\infty}\le 1,\ \mathbf{a}_k^T=\begin{bmatrix}a_{kx} & a_{kz} & a_{ky}\end{bmatrix}, \tag{18}$$

where $\delta\mathbf{r}_d$ is a zero-mean random component, to be kept as negligible with respect to the periodic component, since $\mathbf{g}(\theta)$ is not rejected. As the forcing frequency $\underline{\omega}$ is very close to $\underline{\omega}_z$ and $\underline{\omega}_y$, forcing (17) with a series like (18) generates a bounded beat motion as mentioned in Section 2.2 and proved by high-fidelity simulation (Fig. 3). The series coefficients follow from the closed-loop transfer functions in (15), and from expanding $\mathbf{g}(\theta)$ as in (18): they are parameterized by the control gains in (14). An approximate, worst-case solution is adopted. The tracking error coefficients in (18) are kept equal to their peak values, which makes them independent of the control gains. Inserting (18) in (14) provides a series expansion of $\Delta\mathbf{u}(t)$ with coefficients depending on the control gains. Using this series in (11) the first design inequality is obtained.

The second design inequality is achieved by showing that only inequality (13) affects control gains, whereas inequality (12) decides sensor and actuator noise. In fact $\mathbf{V}$ is a low-pass filter whose high-frequency asymptote is shaped by K_r and K_v; moreover the bandwidth of $\mathbf{V}$ must be sufficiently smaller than the lower limit f_0 of the MBW (9) so as to guarantee (13). This is formulated by the limit

$$\lim_{f>f_0}\left(I-\mathbf{V}(jf)\right)\to I, \tag{19}$$

and by the fact that $\mathbf{S}_a^2(f)$ in (12) is just the spectral density of the wide-band noise $\mathbf{w}_a$ in (15). The latter sums up high-frequency accelerometer, thruster and sensor noise, and allows to allocate them. Using (16), and observing that $\mathbf{S}(jf)$ satisfies a limit like (19), the high-frequency asymptote holds

$$\lim_{f>f_0}\mathbf{V}(jf)=\lim_{f\to\infty}\mathbf{C}(jf)\mathbf{M}(jf)=$$
$$=\frac{K_v}{j2\pi f}\begin{bmatrix}1 & -\underline{\omega}\left(j\pi f\right)^{-1} & 0\\ \underline{\omega}\left(j\pi f\right)^{-1} & 1 & 0\\ 0 & 0 & 1\end{bmatrix}. \tag{20}$$

Next step is to find a suitable parameterization of the control gains, making feasible the solution of (11) and (13).

3.4 Decoupled closed-loop eigenvalue design

Control gain parameterization passes through a decoupled eigenvalue design and the closed-loop Hill's equation properties. To this end, rearrange the controllable part of (3) and the control law (14) as

$$\begin{bmatrix}\dot{\mathbf{x}}_x\\ \dot{\mathbf{x}}_z\\ \dot{\mathbf{x}}_y\end{bmatrix}(t)=\begin{bmatrix}A_{xx} & A_{xz} & 0\\ A_{zx} & A_{zz} & 0\\ 0 & 0 & A_{yy}\end{bmatrix}\begin{bmatrix}\mathbf{x}_x\\ \mathbf{x}_z\\ \mathbf{x}_y\end{bmatrix}+\begin{bmatrix}B\left(\Delta u_x+x_{dx}+w_{ax}+g_x\right)\\ B\left(\Delta u_z+x_{dz}+w_{az}+g_z\right)\\ B\left(\Delta u_y+x_{dy}+w_{ay}+g_y\right)\end{bmatrix},$$
$$\begin{bmatrix}\Delta u_x\\ \Delta u_z\\ \Delta u_y\end{bmatrix}=-\begin{bmatrix}K_{xx} & K_{xz} & K_{xy}\\ K_{zx} & K_{zz} & K_{zy}\\ K_{yx} & K_{yz} & K_{yy}\end{bmatrix}\begin{bmatrix}\mathbf{x}_x\\ \mathbf{x}_z\\ \mathbf{x}_y\end{bmatrix}-\begin{bmatrix}x_{dx}\\ x_{dz}\\ x_{dy}\end{bmatrix} \tag{21}$$

with the following matrices and vectors

$$A_{xx}=\begin{bmatrix}1 & 1\\ 0 & 1\end{bmatrix},\ A_{xz}=\begin{bmatrix}-2\underline{\omega} & 0\\ 0 & 0\end{bmatrix},\ B=\begin{bmatrix}0\\ 1\end{bmatrix}$$
$$A_{zx}=\begin{bmatrix}0 & 0\\ 0 & 2\underline{\omega}\end{bmatrix},\ A_{zz}=\begin{bmatrix}1 & 1\\ -\underline{\omega}_z^2 & 0\end{bmatrix},\ A_{yy}=\begin{bmatrix}1 & 0\\ -\underline{\omega}_y^2 & 0\end{bmatrix}. \tag{22}$$
$$\mathbf{x}_x=\begin{bmatrix}\delta x\\ \Delta v_a\end{bmatrix},\ \mathbf{x}_z=\begin{bmatrix}\delta z\\ \Delta v_z\end{bmatrix},\ \mathbf{x}_y=\begin{bmatrix}\delta y\\ \Delta v_y\end{bmatrix}$$

The first step is to fix closed-loop eigenvalues that guarantee bounded-input-bounded-output stability to (21) and (14). Following Lemma 1 and the decoupling inequality (13), the following closed-loop eigenvalues are fixed

$$\lambda_{x0}=-p_{x0}<0,\ \lambda_{x1}=-p_{x1}<0$$
$$\lambda_{z0,z1}=\left(-\zeta_z\pm j\sqrt{1-\zeta_z^2}\right)\underline{\omega}_z,\ \lambda_{y0,y1}=\left(-\zeta_y\pm j\sqrt{1-\zeta_y^2}\right)\underline{\omega}_y, \tag{23}$$

where the first pair refers to longitudinal motion that must be bounded in position and rate, the second and third to radial and cross-track displacements which must be weakly damped not to degrade gravitational components.

Feedback gains guaranteeing (23) follow from the results below. The first one is immediate.

Result 1. Since cross-track dynamics in (21) is fully decoupled from longitudinal and radial dynamics, the feedback matrix in (21) reduces to

$$K=\begin{bmatrix}K_{xx} & K_{xz} & 0\\ K_{zx} & K_{zz} & 0\\ 0 & 0 & K_{yy}\end{bmatrix}. \tag{24}$$

Cross-track gains derive from a well-known result, which is stated without proof (see Canuto, 2010b).

Result 2. Assuming $\left|g_y+w_{ay}\right|_{\infty}$ is bounded, a feedback matrix $K_{yy}=\begin{bmatrix}k_{ry} & k_{vy}\end{bmatrix}$ which stabilizes $A_{yy}-BK_{yy}$, and bounds $\left|\Delta u_y\right|$ in agreement with (11), is a damping feedback

$$k_{ry}=0,\ k_{vy}=2\zeta_y\underline{\omega}_y, \tag{25}$$

where $\zeta_y>0$ must be selected to be compatible with (13).

In order to apply Result 2 to radial feedback, i.e. to fix

$$k_{rz}=0,\ k_{vz}=2\zeta_z\underline{\omega}_z, \tag{26}$$

in $K_{zz}=\begin{bmatrix}k_{rz} & k_{vz}\end{bmatrix}$, longitudinal and radial closed-loop dynamics in (21) must possess a decoupling property.

Lemma 2 and Result 3 provide the feedback gain properties of the closed-loop matrix

$$\left[\begin{array}{c|c} A_{xx}-BK_{xx} & A_{xz}-BK_{xz} \\ \hline A_{zx}-BK_{zx} & A_{zz}-BK_{zz} \end{array}\right] \quad (27)$$

that ensure decoupling. The next Lemma follows from the characteristic polynomial of (27).

Lemma 2. A necessary and sufficient condition for the eigenvalues of (27) are equal to the eigenvalues of the diagonal matrices in (27), is

$$\left(A_{zx}-BK_{zx}\right)\left(\lambda I-A_{xx}+BK_{xx}\right)^{-1}\left(A_{xz}-BK_{xz}\right)=0 \quad (28)$$

Straightforward algebra in (28) and (22) leads to a pair of first-degree polynomials in λ, namely

$$\begin{array}{l} \lambda\left(2\underline{\omega}k_{rzx}+k\left(\underline{\omega}\right)k_{rxz}\right)+2\underline{\omega}\left(k_{rzx}k_{vx}-k\left(\underline{\omega}\right)k_{rx}\right)+k_{rxz}k_{rzx}=0 \\ \left(k\left(\underline{\omega}\right)\lambda+k_{rzx}\right)k_{vxz}=0,\ k\left(\underline{\omega}\right)=k_{vzx}-2\underline{\omega} \end{array} ,(29)$$

which must be solved for the four gains in $K_{xz}=\left[k_{rxz}\quad k_{vxz}\right]$ and $K_{zx}=\left[k_{rzx}\quad k_{vzx}\right]$. A pair of solutions exist, but only one of them allows to bound $\left|W_u\Delta\mathbf{u}\right|_\infty$ (Canuto, 2010b), namely

$$k_{rxz}=k_{rzx}=k_r=-\underline{\omega}k_{vx}\left(1\pm\sqrt{1-4k_{rx}/k_{vx}^2}\right),\ k_{vzx}=k_{vxz}=0 \quad .(30)$$

By adopting (30), the following result follows.

Result 2. Feedback gains (25), (26) and (30) lead to a control law which can be fully tuned through four parameters: the damping coefficients ζ_y,ζ_z, and the eigenvalues $\left\{\lambda_{xj}=-p_{xj}\right\}$, $j=0,1$, which latter set the gains in $K_{xx}=\left[k_{rx}\quad k_{vx}\right]$.

Proof. The proof follows by writing

$$k_{rx}=p_{x0}p_{x1},\ k_{vx}=p_{x0}+p_{x1}, \quad (31)$$

and by observing the non-zero gain in (30) is minimized by

$$k_r=-2p_x\underline{\omega},\ p_x=\min\left\{p_{x0},p_{x1}\right\}. \quad (32)$$

Then $\Delta\mathbf{u}$ becomes fully tunable, since also the rejected disturbance $\mathbf{x}_d$ might be suitably filtered if the case:

$$\begin{array}{l} \Delta u_x=-p_{x0}p_{x1}\delta x-\left(p_{x0}+p_{x1}\right)\Delta v_x+2\underline{\omega}p_x\delta z-x_{dx} \\ \Delta u_z=-2\zeta_z\underline{\omega}_z\Delta v_z+2\underline{\omega}p_x\delta x-x_{dz} \\ \Delta u_y=-2\zeta_y\underline{\omega}_y\Delta v_y-x_{dy} \end{array} . \quad (33)$$

In the following the design parameters are reduced to the pair

$$\zeta=\zeta_y=\zeta_z,\ p_x=p_{x0}=p_{x1}, \quad (34)$$

and the orbit frequencies are simplified to be equal, i.e.

$$\underline{\omega}=\underline{\omega}_z=\underline{\omega}_y. \quad (35)$$

Simulated gains account for different orbit frequencies.

3.5 Gain tuning

Assuming (35), the control law (33) is employed to solve inequalities (11) and (13) for the final parameters in (34). Start from the command inequality (11) which upon (33) and (18), can be rewritten as

$$\begin{array}{l} \left|\Delta u_x\right|\le p_xw_{rx}^{-1}\delta r_{\max}\sum_{k=1}^{\infty}\left(\left(p_x+2\underline{\omega}k\right)\left|a_{kx}\right|+p_x2\underline{\omega}\left|a_{kz}\right|w_{rx}\right)+ \\ +x_{d,\max}\le w_{ux}^{-1}\Delta u_{\max} \\ \left|\Delta u_z\right|\le 2\underline{\omega}\delta r_{\max}\sum_{k=1}^{\infty}\left(k\underline{\omega}\zeta\left|a_{kz}\right|+p_x\left|a_{kx}\right|w_{rx}^{-1}\right)+x_{d,\max}\le\Delta u_{\max} \\ \left|\Delta u_y\right|\le 2\underline{\omega}^2\zeta\delta r_{\max}\sum_{k=1}^{\infty}k\left|a_{ky}\right|+x_{d,\max}\le\Delta u_{\max} \end{array} , \quad (36)$$

where $x_{d,\max}$ is the uniform bound to the entries of $\mathbf{x}_d$, mainly depending on the accelerometer bias in Table 1.

A first-trial solution is found by assuming the longitudinal pole much smaller than the orbit frequency, i.e. $p_x<<2\underline{\omega}$, which simplifies the first inequality in (36) to

$$p_xw_{rx}^{-1}\delta r_{\max}\sum_{k=1}^{\infty}2\underline{\omega}k\left|a_{kx}\right|\le w_{ux}^{-1}\Delta u_{\max}-x_{d,\max}. \quad (37)$$

Allocating the same bound to terms of $\left|\Delta u_z\right|$, assuming 1st and 2nd harmonics to dominate (36), and the higher harmonics to roll down with -40 dB/dec, which implies

$$\sum_{k=1}^{\infty}k\left|a_{kj}\right|\le\gamma<2,\ j=x,y,z, \quad (38)$$

the solution splits into

$$\begin{array}{l} \zeta\le\left(\Delta u_{\max}-x_{d,\max}\right)\left(2\underline{\omega}^2\delta r_{\max}\gamma\right)^{-1}\cong 5\times10^{-3} \\ p_x\le\left(\Delta u_{\max}-x_{d,\max}\right)w_{rx}\left(4\underline{\omega}\delta r_{\max}\right)^{-1}\cong 10^{-3}\ \text{rad/ms}<<2\underline{\omega} \end{array} .(39)$$

The above values may be iterated versus actual position bounds, thus relaxing the worst-case assumption leading to (36). Since as Fig. 3 shows, the along-track component δx can be bounded as δz below $\delta r_{\max}$, one might fix $w_{rx}\cong 1$ in (10) and (39), thus leading to a faster pole.

Consider now inequality (13), which, having observed that the maximum in (13) occurs at $f=f_0$, i.e. on the left border of the MBW in (9), and employing (20), (25), (26) (31), (34) and (35), is rewritten as

$$\sigma_{\max}\left(\frac{-j}{\pi f_0}\begin{bmatrix} p_x & j\alpha p_x & 0 \\ -j\alpha\underline{\omega}\zeta & \zeta\underline{\omega} & 0 \\ 0 & 0 & \zeta\underline{\omega}\end{bmatrix}\right)\le\sigma_{h,\max},\ \alpha=\left(\pi f_0\right)^{-1}\underline{\omega}<1 . \quad (40)$$

Direct computation shows the max singular value in (40) is bounded as

$$\left(\pi f_0\right)^{-1}\sqrt{\left(p_x^2+\zeta^2\underline{\omega}^2\right)\left(1+\alpha^2\right)}\le\sigma_{h,\max}, \quad (41)$$

which yields a further design inequality. If the values from (39) and (13) satisfy (41), as in this case, the first-trial design is complete. Note however that increasing w_x and therefore p_x as suggested above may not respect (41).

4. SIMULATED RESULTS

4.1 Simulated conditions

Simulated results have been obtained from an in-house fine simulator and have been confirmed by the mission end-to-end simulator. A sun-synchronous orbit has been simulated; the initial parameters are: inclination $i=1.69$ rad, eccentricity $e_0=0.002$, geodetic altitude $h_0=325$ km, right ascension of the ascending node $\Omega_0=1.98$ rad. To experience the worst-case low-Earth-orbit environment, an extreme solar activity index, $F_{10.7}=380\times10^{-22}$ W/m^2/Hz, has been assumed, partly mitigated by average geomagnetic index $A_p=20$ nT.

Formation has been assumed to be already achieved. Simulation lasted more than 5 Ms (about 2 months) so as to experience the formation beat motion generated by eccentricity and J2 as expected. The accelerometer noise spectral density is bowl-shaped and can be found in Canuto

and Massotti (2009). Below 1 mHz, a 2nd order drift sets-up, which must be counteracted by formation control. Drift range is much lower than bias as Table 1 shows. The whole suite of drag-free, formation and attitude control has been implemented, including reference generators, state predictors and control laws.

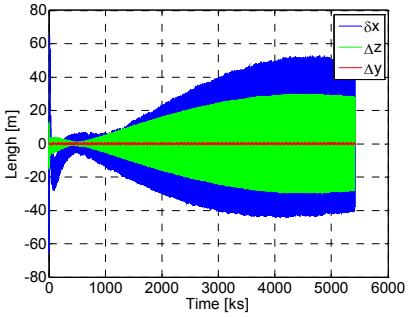

Fig. 3. Residual relative position during 2-month mission.

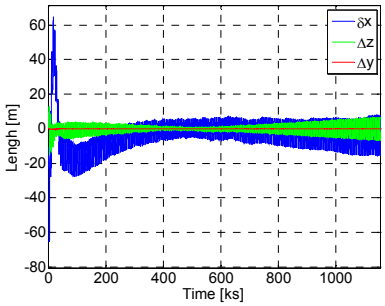

Fig. 4. Enlargement of the onset in Fig. 3.

The relative position residuals during a 2-month mission are shown in Fig. 3. The formation is assumed to start within the bounds (10) and close to a minimum (500 ks) of the beat motion. Then the latter naturally increases (and then decreases) inside the formation bounds: formation control must not reduce it, not to reach command saturation and degrade gravitational components. The long-term oscillation in Fig. 3 modulates the amplitude of the orbit oscillations; the latter ones have a period of $2\pi / \underline{\omega} \cong 5400$ s. Fig. 4 shows the enlargement of Fig. 3 at the simulation onset. The initial peak allows tracking the accelerometer bias. Closed-loop time constants are very long and are imposed by the low thrust limits in Table 1 as explained in Section 3. A gain scheduling has been implemented, the wide-band phase terminating at 600 ks. This is better appreciated in Fig. 5.

4.2 Simulated performance

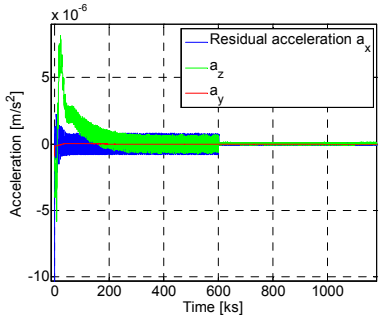

Fig. 5. Residuals from wide- to narrow-band control.

Fig. 5 shows the residual non-gravitational acceleration that must respect the drag-free bound in (12). During bias tracking until 600 ks, the latter is not respected. Fig. 2 shows the spectral density of the 3D components of the residual non gravitational acceleration since 600 ks, when the narrow-band control has been applied after bias tracking, so as to ensures zero-mean relative position. Overshoots below the MBW frequency limit of 1 mHz, are due to non-zero radial and cross-track damping, spilling orbit harmonics into formation command, but respecting (13).

5. CONCLUSIONS

The paper outlines the formation control design and the simulated results, constrained by low command authority, formation box, drag-free bounds below 0.01 μm/s^2 in a mid frequency band around 1 mHz, and command decoupling from periodic input perturbations due to tide forces. Coupled with a low-Earth orbit and 10-km distance formation, the above requirements make the control design and the relevant technology challenging. The paper shows that formation fluctuations can be kept within the required box, also under worst-case environment conditions. They compete with formation control authority at the level of drag-free and attitude control, because of an all-propulsion mission. Further developments concern formation acquisition and GPS/optical metrology sensor fusion.

REFERENCES

Canuto, E. (2007) Embedded Model Control: outline of the theory. *ISA Trans*. **46** (3), 363-377.

Canuto, E (2008) Drag-free and attitude control for the GOCE satellite. *Automatica,* **44**, 1766-1780.

Canuto, E. and Massotti, L. (2009) All-propulsion design of the drag-free and attitude control of the European satellite GOCE. *Acta Astronautica*, **64**, 325-344.

Canuto, E, Molano, A. and Massotti, L. (2010a) Drag-free control of the GOCE satellite: noise and observer design. *IEEE Trans. on Control System Techn.,* **18** (2), 501-509.

Canuto, E. et al. (2010b) Long-distance, drag-free, low-thrust, low-Earth-orbit, formation control, *Proc. 18th IFAC Workshop on Automatic Control in Aerospace (ACA 2010)*, Nara, Japan, September 6-10, pp. 1-6.

Canuto, E. et al. (2011) Long-distance, drag-free, low-thrust, LEO formation control for the Earth gravity monitoring, submitted to *Acta Astronautica*.

Kapila, V., Sparks, A.G., Buffington, J.M. and Yan Q. (2000) Spacecraft formation flying: dynamics and control, *J. Guidance, Control and Dyn.* **23** (2), 561–564.

Inalhan, G., Tillerson, M. and How, J.P. (2002) Relative dynamics and control of spacecraft formations in eccentric orbits. *J. Guid., Control & Dyn.,* **25** (1), 48-60.

Rossi, M. and Lovera, M. (2002) A Predictive Approach to Formation Keeping for Constellations of Small Spacecrafts in Elliptical Orbits, *Proc. 5th Int. ESA Conf. on GNC Systems*, October 22-25, Frascati, Italy.

Schweighart S.A. and Sedwick R.J. (2002) High-Fidelity Linearized J2 Model for Satellite Formation Flying, *J. of Guidance, Control and Dynamics*, **25** (6), .

Xu, Y. et al. (2007) μ control for satellite formation flying, *J. Aerospace Engineering,* 10-21.